MATERIALS RESEARCH LETTERS

Taylor & Francis
Taylor & Francis Group

ORIGINAL REPORTS

🔓 OPEN ACCESS | Check for updates

One-step synthesis of high-entropy diborides with hierarchy structure and high hardness via aluminum-melt reaction method

Jinfeng Nie[a], Yating Zhi[a], Yong Fan[a], Yonghao Zhao[a,b] and Xiangfa Liu[c]

[a]Nano and Heterogeneous Materials Center, School of Materials Science and Engineering, Nanjing University of Science and Technology, Nanjing, People's Republic of China; [b]School of Materials Science and Engineering, Hohai University, Changzhou, China; [c]Key Laboratory for Liquid–Solid Structural Evolution and Processing of Materials, Ministry of Education, Shandong University, Jinan, People's Republic of China

ABSTRACT
Two new high-entropy metal diborides $(ZrTiVCr)B_2$ and $(ZrTiVCrMn)B_2$ were successfully synthesized via a novel aluminum melt reaction method. The high-entropy diboride crystals have a hexagonal structure and possess high compositional uniformity. We unexpectedly found that the Mn elements could significantly change the crystal morphology of $(ZrTiVCrMn)B_2$, resulting in a hierarchically structured nanosheet-assembled nanoplatelet shape. Benefiting from this interesting hierarchical structure and enhanced lattice distortion, the average hardness of the $(ZrTiVCrMn)B_2$ phase is significantly enhanced to 31.44 GPa as compared to that of $(ZrTiVCr)B_2$ for 28.82 GPa. This work will supply a new paradigm for synthesizing high-entropy metal diborides.
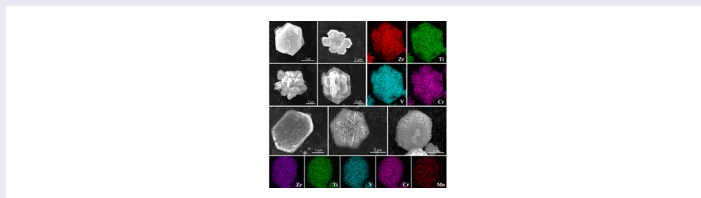
IMPACT STATEMENT
This work reports that two new high-entropy metal diborides $(ZrTiVCr)B_2$ and $(ZrTiVCrMn)B_2$ with ultrahigh hardness have been successfully synthesized via a novel one-step synthesis method in aluminum melt.

In 2004, Yeh et al. and Cantor et al. proposed the concept of high-entropy alloys simultaneously, which are single-phase solid solutions composed of five or more elements with equimolar or nearly equimolar ratios. Benefiting from the four core effects, i.e. high entropy, lattice distortion, slow diffusion, and cocktail effect, high-entropy alloy exhibit some unique properties, which have attracted extensive interest and become one of the research hotspots in the field of metallurgy [1,2]. Inspired by this concept, researchers extended the concept of high entropy to ceramic materials. High-entropy ceramics are single-phase ceramic materials composed of four or more anions and cations [3]. Up to now, the types of high-entropy ceramics that have been reported include high-entropy oxides (HEO)[4,5], high-entropy borides(HEB)[6–9], high-entropy carbides(HEC)

[10,11] and high-entropy nitrides(HEN) [12], etc., are widely used in cutting tools, ultra-high-speed aircraft, catalytic and energy materials [13–16]. Among these ceramics, high-entropy diborides have attracted great interest. Gild [8] et al. revealed that high-entropy diborides exhibited higher hardness and better oxidation resistance. Wen [17] et al prepared $(Hf_{0.28}Zr_{0.28}Ta_{0.28}W_{0.15})B_2$ with superior oxidation resistance at 1473 ∼ 1773K.

At present, the research on high-entropy diborides is mainly focused on preparation and synthesis methods to gain high-purity and superfine high entropy boride ceramic [18]. Tallarita et al. [19] utilized the Self-propagating High-temperature Synthesis (SHS) method to first synthesize the $(HfMoTaNbTi)B_2$ powders using pure metal and pure B powder as raw materials. The
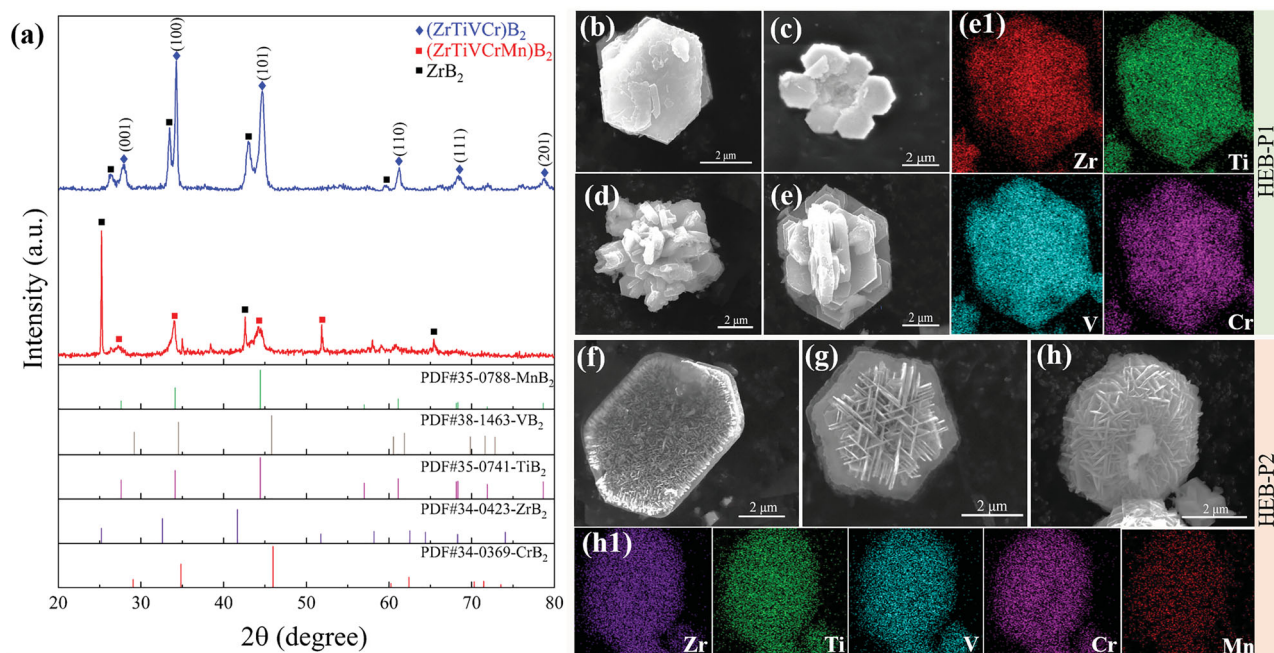
Figure 1. (a) XRD patterns of extracted high entropy based ceramic powders in HEB-1 and HEB-2; and their typical morphology: (b-e) $(ZrTiVCr)B_2$; (f-h) $(ZrTiVCrMn)B_2$; (e1, h1) the EDS mapping of different elements.

synthesized powder was subsequently consolidated at 1950 °C for 20 min via Spark Plasma Sintering (SPS) to obtain the bulk, while its density is only approximately 92.5%. This is mainly due to the large particle size of the powders synthesized by SHS, which is not beneficial to sintering. Liu [13] et al. used the borothermal reduction method to synthesize ultrafine high-entropy boride powders $(Hf_{0.2}Zr_{0.2}Ta_{0.2}Nb_{0.2}Ti_{0.2})B_2$ with a particle size of 300 nm. They also used the boro/carbothermal reduction to synthesize high-purity $(Hf_{0.25}Ta_{0.25}Nb_{0.25}Ti_{0.25})B_2$ powders with a particle size of 200–300 nm [15]. Zhang [20] et al. first synthesized $(Zr_{0.2}Ta_{0.2}Ti_{0.2}Nb_{0.2}Hf_{0.2})B_2$ and $(Zr_{0.2}W_{0.2}Ti_{0.2}Mo_{0.2}Hf_{0.2})B_2$ using metal oxides and boron powder as raw materials by borothermal reduction method. Then, high-entropy boride bulk $(Zr_{0.2}Ta_{0.2}Ti_{0.2}Nb_{0.2}Hf_{0.2})B_2$ and $(Zr_{0.2}W_{0.2}Ti_{0.2}Mo_{0.2}Hf_{0.2})B_2$ with a high density of $\sim 94.0\%$ were prepared via SPS at 2000 °C, while the composition is found to be non-uniform. It shows that the primary challenges of the current synthesis methods, such as energy and time-consuming, the residual oxides, and the relatively complex preparation process, have affect the properties of high-entropy diboride to different extents.

In this work, we report a novel synthesis method of high-entropy diboride microcrystals utilizing in-situ reactions in aluminum melt. Vacuum arc melting can melt some refractory metals with a melting point higher than 4000 K, and can screen out a combination of elements that are conducive to the synthesis of high-entropy diborides in a short time [21]. At present,

the element selection of the synthesized high-entropy diborides is mainly concentrated on the transition group metals which are in the IVB group, VB group, and VIB group, such as Hf, Ta, Nb, etc. These elements are noble metal elements, and the cost is high, which greatly limits the scope of their further wide application. In this work, we have successfully synthesized $(ZrTiVCr)B_2$ and $(ZrTiVCrMn)B_2$ in the aluminum melt via the arc melting method. Furthermore, the crystal morphology and growth mechanism of the high-entropy diboride were revealed. It is found that the hierarchical structure and enhanced hardness have been achieved with trace Mn dopant, which provides a new paradigm for the design and synthesis of high-entropy diborides.

Two samples Al-3.74$(ZrTiVCr)B_2$ and Al-3.72$(ZrTiVCrMn)B_2$ containing different high-entropy diboride particles were prepared via a melt reaction method, named HEB-1 and HEB-2, and their nominal composition and detail preparation method are shown in the Supplementary Materials. The high-entropy diboride powders extracted from these two samples are named HEB-P1 and HEB-P2, respectively. The experimental procedure and analytical methods were also described in detail in the Supplementary Materials. The microstructures of HEB-1 and HEB-2 and the corresponding EDS analysis of the as-synthesized high-entropy diboride phases in the aluminum matrix are shown in Fig. S1 in the supplementary materials. Besides, the morphologies of the synthesized high-entropy diboride particles extracted from the matrix of these two samples are shown in Fig.

Table 1. Calculated lattice parameters of $(ZrTiVCr)B_2$ and $(ZrTiVCrMn)B_2$ according to XRD patterns

Samples	2θ	d (Å)	hkl	a (Å)	c (Å)
$(ZrTiVCr)B_2$	27.86	3.199	001	3.019	3.199
	34.27	2.614	100		
	44.66	2.027	101		
$(ZrTiVCrMn)B_2$	27.26	3.268	001	3.042	3.268
	34.00	2.635	100		
	44.22	2.049	2.049		

S2. Figure 1(a) shows the XRD diffraction patterns of the as-synthesized high entropy based ceramic powders extracted from the aluminum matrix. It indicates that $(ZrTiVCr)B_2$ and $(ZrTiVCrMn)B_2$ phases have been successfully synthesized and these high-entropy diborides show a hexagonal structure. Meanwhile, it is noticed that a small amount of ZrB_2 existed and was shown in the XRD patterns. It is considered that the formation of ZrB_2 is due to the low mixing enthalpy of Zr and B and also the insufficient reaction in the present experimental condition. The mixing enthalpy between the atoms involved in the present system is shown in Table S1. During the in-situ melt reaction, the dissolved boron atoms in the melt readily react with dissolved Zr atoms and then form ZrB_2. Thus, it is expected that the composition in the as-synthesized HEB will be non-equimolar although the raw powders of Zr, Ti, V, Cr, Mn are equimolarly mixed. It is noticed that the diffraction peaks of the two high-entropy diborides are much wider than the conventional metal diborides, indicating severe lattice distortion existed in the crystal structure induced by these multiple atoms. The lattice parameters are calculated as shown in Table 1. For $(ZrTiVCr)B_2$, the lattice parameters a and c were 3.019 and 3.199 Å, both of which are slightly smaller than the average lattice parameters (3.042, 3.222 Å). For $(ZrTiVCrMn)B_2$, the lattice parameters a and c were 3.042 and 3.268 Å, both of which are slightly larger than the average lattice parameters (3.036, 3.268 Å). Therefore, the lattice parameters are not the average of the individual metal diborides, but are instead the result of energetic optimization of the structure after reaching thermodynamic equilibrium driven by mixing enthalpy and configurational entropy.

Figure 1(b-e) shows the typical SEM images of the $(ZrTiVCr)B_2$ powders extracted from HEB-1. It can be seen that the $(ZrTiVCr)B_2$ exhibits several typical morphologies, i.e. hexagonal plate-like, hexagonal petal-like, and agglomerated plate-like. At a higher magnification, it shows that they are all composed of hexagonal plates as a unit, and the size ranges from 1–5 μm with a thickness of 0.1–0.5μm. The EDS mapping analysis as shown in Figure 1(e1) shows that the elemental distributions are

uniform at the microscale. Figures 1(f-g) show the typical morphologies of $(ZrTiVCrMn)B_2$ powders extracted from HEB-2. Different from the plate-like morphology of the $(ZrTiVCr)B_2$ phase, $(ZrTiVCrMn)B_2$ shows a hierarchically structured hexagonal plate-like morphology, with a size of 1–5 μm. Actually, the hierarchical $(ZrTiVCrMn)B_2$ particle is composed of multiple nano-sized two-dimensional thin platelets, which also exhibit hexagonal symmetry characteristics. It is considered that these thin platelets in situ formed in the melt and then they tend to be vertically self-assembled on a preformed hexagonal thin plate into a hierarchically hexagonal plate, with a large specific surface area [22,23]. The EDS mapping analysis further confirms that the Zr, Ti, V, Cr, and Mn elements are homogeneously distributed in the crystals as shown in Figure 1(h1). It indicates that the Mn element has a significant impact on the crystal growth and morphology of $(ZrTiVCrMn)B_2$.

TEM analysis was carried out to further investigate the crystal structure of the synthesized high-entropy diboride powders. Figure 2(a) shows a typical TEM image of $(ZrTiVCr)B_2$ powder. According to the corresponding selected area electron diffraction (SAED) pattern along the crystal axis [0001] as shown in the inset of Figure 2(a), it further demonstrates that the $(ZrTiVCr)B_2$ hexagonal plate is a single crystal and has an h.c.p. crystal structure. The high-resolution transmission electron microscope (HRTEM) images are shown in Figures 2(b, c), it indicates that the synthesized $(ZrTiVCr)B_2$ ceramic powder has a periodic lattice structure and the calculated interplanar spacing of $10\bar{1}0$ planes is 0.275 nm. Figure 2(e) shows a typical TEM image of $(ZrTiVCrMn)B_2$ powder, which shows a hierarchical structure composed of thin two-dimensional nanoplatelets and agrees well with the SEM image. The corresponding SAED pattern is shown in the inset of Figure 2(e), and it can be clearly seen that the $(ZrTiVCrMn)B_2$ particle is still a single crystal with a hexagonal structure, which indicates that the Mn dopant only induced the crystal morphology change, but its crystal structure does not vary. Figure 2(f, g) shows the HRTEM images of $(ZrTiVCrMn)B_2$. It shows that the synthesized powder has a periodic lattice structure and the interplanar spacing of $10\bar{1}0$ planes is 0.276 nm. For comparison, the interplanar spacing of $10\bar{1}0$ planes for the $(ZrTiVCr)B_2$ is close to that of $(ZrTiVCrMn)B_2$ with the introduction of trace Mn, while both are slightly larger than the values calculated from the XRD result.

To evaluate the lattice distortions in the crystal structure, the local structural strain fields can be obtained by geometric phase analysis (GPA) with an accuracy of 0.003 nm. The structural strain field images of the $(ZrTiVCr)B_2$ and $(ZrTiVCrMn)B_2$ corresponding to the high-resolution images of Figure 2b and f are shown in
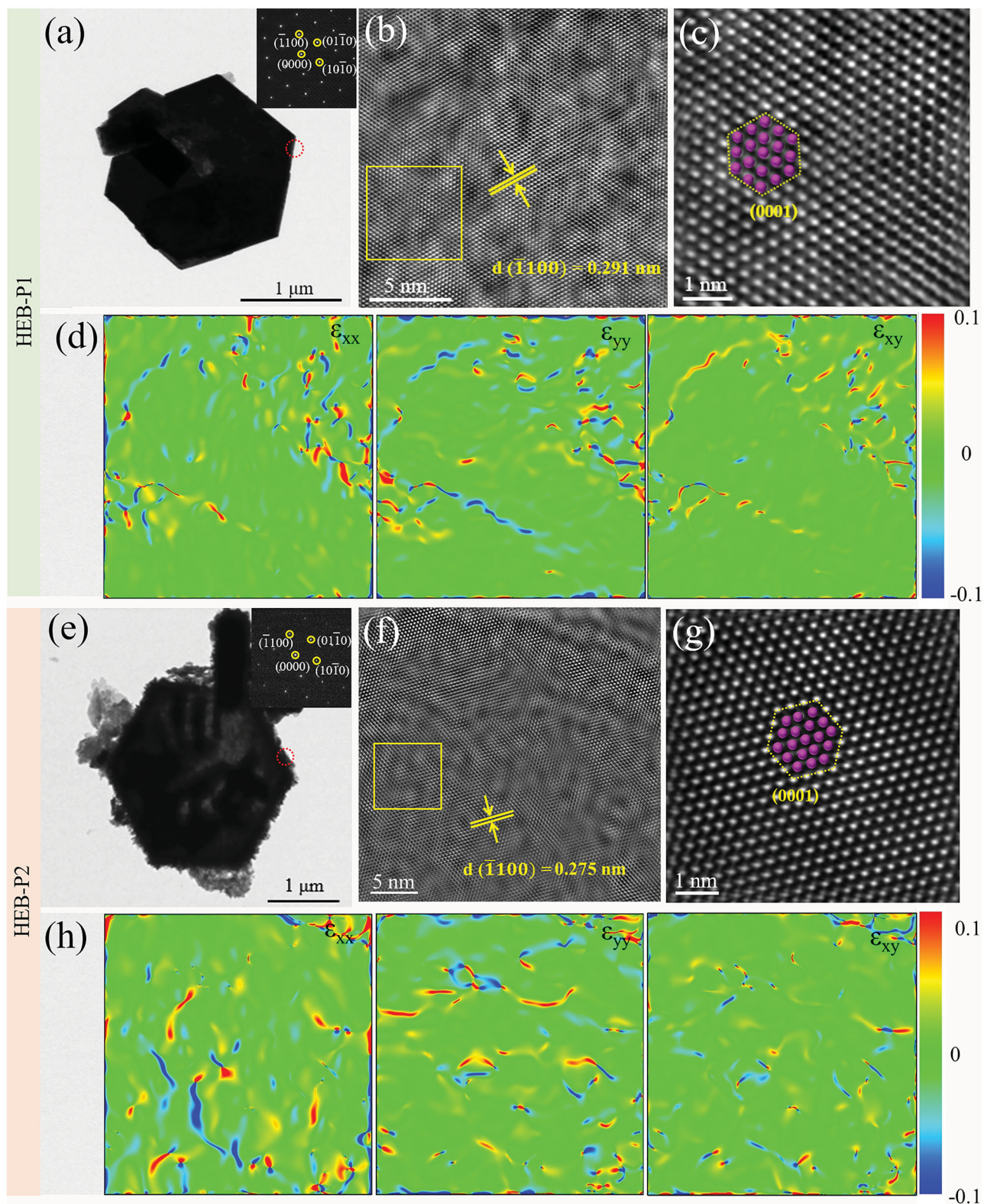
Figure 2. TEM images, the corresponding SAED patterns, HRTEM image, and the corresponding strain field analysis processed by GPA of the high entropy diborides: (a-d) (ZrTiVCr)B$_2$; (e-h) (ZrTiVCrMn)B$_2$.

Figure 2(d, h), respectively. Red color represents positive strain and blue color represents negative strain. As shown in Figure 2(d, h), some areas are covered by red and blue. It proves that lots of nanoscale structural distortions formed in these two crystals, which is consistent with the lattice distortion effects of high entropy diborides. Compared with the strain distributions in these two high-entropy diborides, it indicates that the lattice distortion effect in the (ZrTiVCrMn)B$_2$ is larger than that of (ZrTiVCr)B$_2$ due to the introduction of additional Mn element.

Generally, the final crystal morphology depends on two aspects: the inner crystal structure and the external environment during crystal growth. According to the Gibbs-Wuff laws, the equilibrium shape of a crystal is that with the minimum total surface energy, and the faces with lower surface energy will be exposed [24]. It is known that the close-packed facets with higher reticular densities and larger interplanar spacing always have lower surface energy. The Bravais-Frediel law has revealed that the importance (frequency of occurrence) of a crystal face increases with its reticular density and interplanar spacing [25,26]. Therefore, the crystal tends to form the morphology with the lowest surface energy, and the close-packed facet with lower surface energy is easily exposed. For metal diborides, the relative importance of the close-packed planes is $0001 > 10\bar{1}0 > 10\bar{1}1$ [27]. The equilibrium crystal morphology of metal diborides tends to be hexagonal platelets. In this view, the equilibrium crystal morphology of the (ZrTiVCr)B$_2$ and (ZrTiVCrMn)B$_2$ is a hexagonal platelet as displayed in Figure 1(b).

However, further crystal growth depends on the properties of the solid/liquid interface. According to Jackson's theory [28], the solid–liquid interface can be divided into two categories: rough interface and smooth interface. The Jackson factor α is generally used to determine the nature of the interface, α can be expressed as:

$$\alpha = \frac{\Delta H}{RT}\frac{\eta 1}{Z} \qquad (1)$$

Where ΔH is enthalpy changes, η_1/z is the fraction of the nearest neighbor sites which are in a single layer of molecules at the surface, T is the temperature, and R is the gas constant.

When $\alpha \leq 2$, the interface is rough and it is smooth when $\alpha > 2$ [28]. For metal diborides, the α values of $0001, 10\bar{1}0$ and $10\bar{1}1$ are greater than 4. Thus, it can be inferred that the α values of these planes for high-entropy metal diborides are also larger than 4 [29,30]. Therefore, the solid–liquid interface of high-entropy diboride is a smooth interface, which indicates that its growth will be controlled by two-dimensional nucleation [31,32]. As

shown in Figure 1(b-e), the growth steps can be seen clearly on (ZrTiVCr)B$_2$ crystals. Song et al. [33] have revealed that the growth of the TiB$_2$ hexagonal plate was a layer-by-layer growth controlled by a two-dimensional nucleation. It was also found that no uniform grains were observed attached to the side and step edges of TiB$_2$ plates, which became finer and disappeared during the growth.

In this work, it is noted that the crystal morphology of (ZrTiVCrMn)B$_2$ has been changed significantly by the Mn dopant and it shows a hierarchical structure composed of oriented aligned nanoplatelets. Although the final morphologies of these two diborides are quite different, the growth unit of (ZrTiVCrMn)B$_2$ is also a hexagonal platelet. These hexagonal platelets aggregate via a self-assembly process in the aluminum melt and then derive the various hierarchical morphologies. The doping of Mn in (ZrTiVCr)B$_2$ only changes the crystal morphology but does not change its hexagonal crystal structure. (ZrTiVCrMn)B$_2$ is still a hexagonal close-packed structure. On one hand, a thinner hexagonal plate is formed for (ZrTiVCrMn)B$_2$, which indicates that the growth rates of $(10\bar{1}0)$ and $10\bar{1}1$ become faster, and the exposed areas of the side region of the hexagonal platelets decreased. Thus it is expected that the introduction of Mn increased the growth rates of $(10\bar{1}0)$ and $10\bar{1}1$ planes. It is also reported in the literature that Mn will selectively adsorb on different surfaces of CrB$_2$ and TiB$_2$ to influence the growth rate of the specific crystal planes to different extent [34,35]. On the other hand, the introduction of Mn promotes the formation of bugles on the hexagonal platelets. Mn element, as a transitional element, has an incomplete outer electron layer that may cause the redistribution of electrons and significantly increase the binding force between atoms when entering the lattice. In addition, as an increased component species, the addition of the element Mn can potentially effectively hinder the diffusion of atoms. As a result, a large number of bulges are formed on the primary crystal, instead of newly formed hexagonal platelets. According to the principle of compositional supercooling, after the formation of the primary crystals, the solute atoms are enriched at the front of the solid–liquid interface, and then a large number of bulges formed on the primary hexagonal platelet, and these protrusions are rapidly extended to the solute-rich region [36]. Compared with new nucleation, it is easier to take the bulges as the substrate and then grow epitaxially. Due to the intrinsic anisotropic characters of hexagonal high entropgy diborides, the aggregated particles would attach orientally to each other to reduce the energy of the system. The surface energy of an individual hexagonal plate is quite high with two exposed planes. Thus, they tend to pile up perpendicularly to the plane to
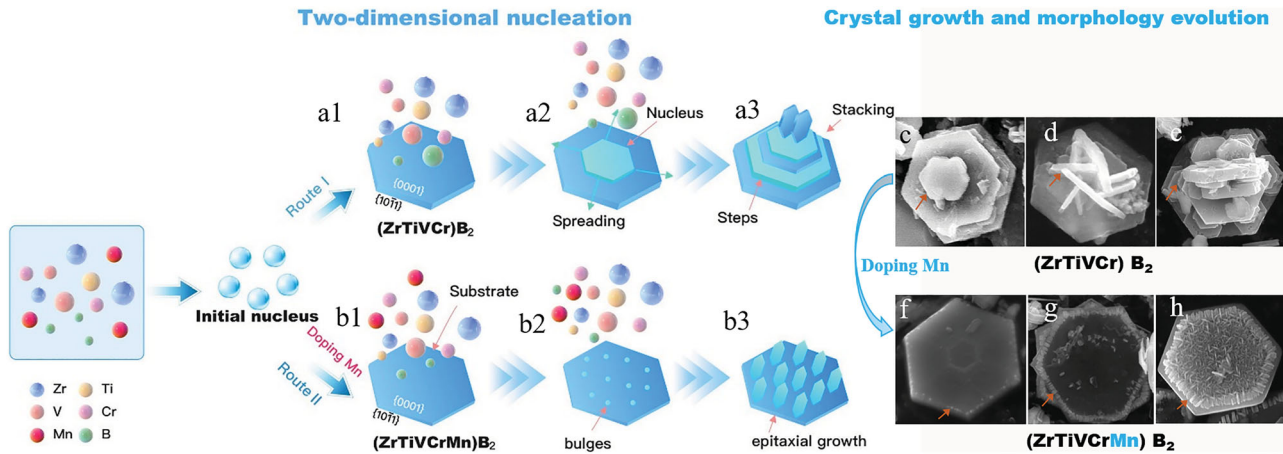
Figure 3. Schematic illustration of the crystal growth and morphology evolution of diborides in the aluminum melt: (a) showing the two-dimensional nucleation of (ZrTiVCr)B$_2$, the spreading growth behavior of the nuclei and the stacking phenomenon; (b) the doping of Mn induced the formation of bulges on the substrate of the (ZrTiVCrMn)B$_2$ and the epitaxial growth behavior; (c-e) the typical SEM images of (ZrTiVCr)B$_2$ crystals; (f-h) the typical SEM images of (ZrTiVCrMn)B$_2$ crystals.
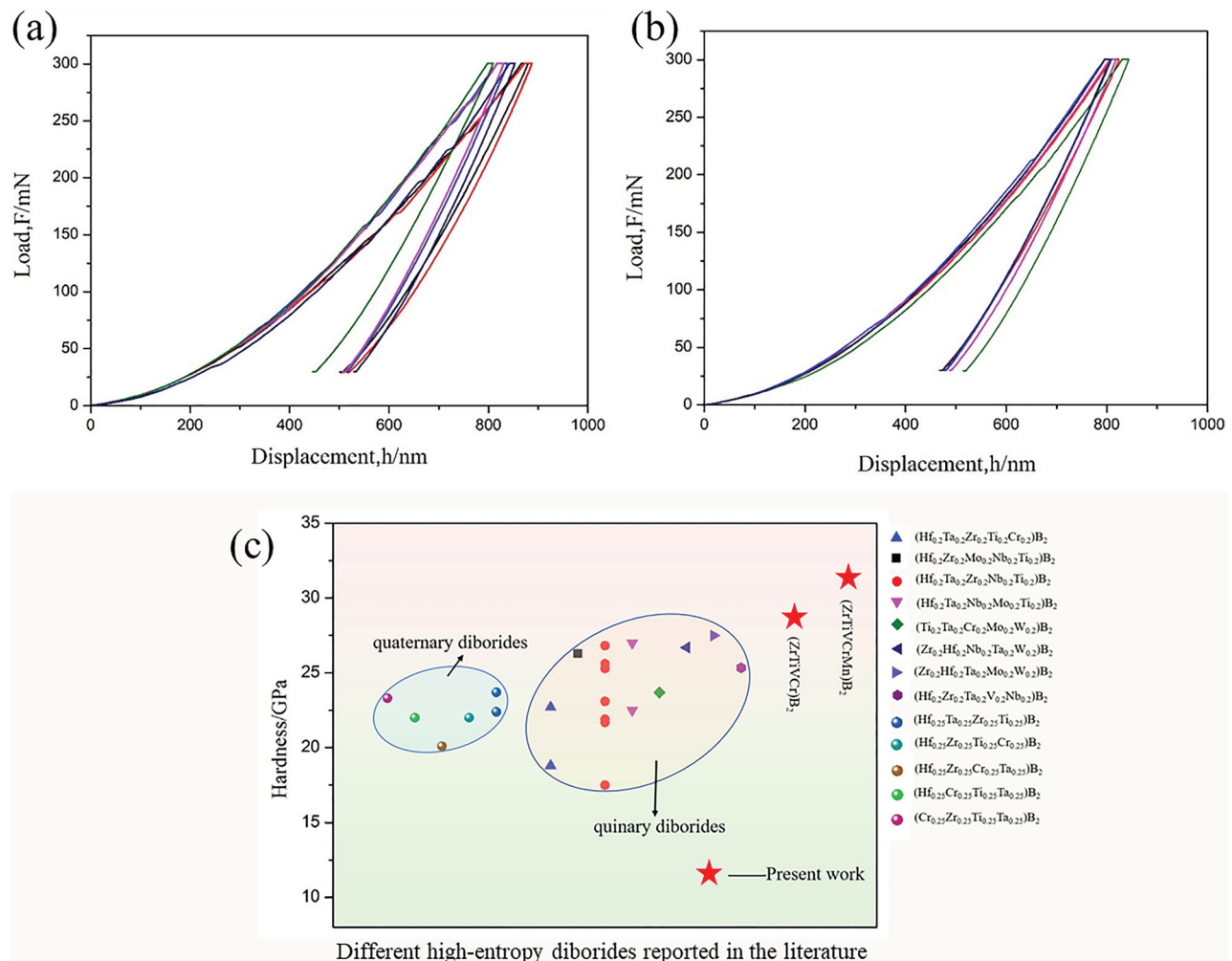

Figure 4. (a, b) The load-displacement curves of (ZrTiVCr)B$_2$ and (ZrTiVCrMn)B$_2$, (c) statistical chart of hardness values of the currently prepared quaternary and quinary high-entropy borides[6,21,37–41].

decrease surface energy by greatly reducing the exposed area.

Based on the above analysis, a schematic diagram of the crystal growth process of $(ZrTiVCr)B_2$ and $(ZrTiVCrMn)B_2$ in the aluminum melt was established, as illustrated in Figure 3. At the initial stage of growth, the high-entropy diboride grows fast and exhibits the characteristics of isotropic growth, displaying a spherical morphology. With further growth, driven by the decrease in Gibbs free energy, a hexagonal plate shape with the lowest surface energy is formed. For the $(ZrTiVCr)B_2$, the crystal growth of the hexagonal platelet is controlled by the two-dimensional nucleation and layer-by-layer growth as illustrated in Figures 3a1 and a2. The corresponding morphology is shown in Figure 3c. While some newly formed hexagonal platelets spread along the basal plane and stacks perpendicular to the basal plane as illustrated in Figure 3a3. The corresponding final derived morphologies are shown in Figures 3d and e. For the $(ZrTiVCrMn)B_2$, a large number of bulges (Figure 3f) are formed on the primary crystal due to the supercooling of the composition as illustrated in Figure 3b2. The bulges act as the nucleating substrate and grow epitaxially, forming a hierarchical structure composed of orientated-aligned nanosized hexagonal-platelet (Figure 3b3). The corresponding final morphologies are shown in Figures 3 g and h.

Figure 4 shows the diagram of the load-displacement curves of the $(ZrTiVCr)B_2$ and $(ZrTiVCrMn)B_2$ bulk ceramic measured by the nanoindenter. According to the Oliver-Pharr method, the average hardness of $(ZrTiVCr)B_2$ and $(ZrTiVCrMn) B_2$ high entropy-based ceramic is calculated to be 28.82 and 31.44 GPa, respectively. It can be seen that the introduction of Mn increases the hardness by about 9.1%, due to the enhanced solid solution strengthening effect. The Mn atoms doped into the crystal lattice as a kind of solute atoms, leading to severe lattice distortion. In addition, the results show that the hardness value of high entropy diboride is greatly affected by the composition. Compared with the other reported quaternary and quinary diboride particles [6,21,37–41], the prepared $(ZrTiVCr)B_2$ and $(ZrTiVCrMn) B_2$ display superior properties. It is considered that the local chemical bonding properties of solid solution will be varied with lattice parameters of different diborides, thereby affecting their hardness [42].

In summary, two new $(ZrTiVCr)B_2$ and $(ZrTiVCrMn)B_2$ high-entropy borides were successfully synthesized utilizing an aluminum melt reaction method for the first time. Both the $(ZrTiVCr)B_2$ and $(ZrTiVCrMn)B_2$ crystals have a hexagonal crystal structure and possess high compositional uniformity. The $(ZrTiVCr)B_2$ powders exhibit three typical morphologies, including hexagonal platelets, hexagonal petals, and agglomerated platelets. Meanwhile, we unexpectedly found that the Mn elements could significantly change the crystal morphology of $(ZrTiVCrMn)B_2$, resulting in a hierarchical structure composed of multiple nanosized two-dimensional hexagonal platelets. The synthesis and growth mechanism of the two new high-entropy diborides is revealed by morphology and atomic lattice structure analysis. Benefiting from this interesting hierarchical structure, the average hardness of the $(ZrTiVCrMn)B_2$ phase is significantly enhanced to 31.44 GPa as compared to that of $(ZrTiVCr)B_2$ about 28.82 GPa. This work will supply a new paradigm for synthesizing high-entropy metal diborides powders.

References

[1] Yeh JW, Chen SK, Lin SJ, et al. Nanostructured high-entropy alloys with multiple principal elements: novel alloy design concepts and outcomes. Adv Eng Mater. 2004;6:299–303. doi:10.1002/adem.200300567

[2] Cantor B, Chang ITH, Knight P, et al. Microstructural development in equiatomic multicomponent alloys. Mater Sci Eng A. 2004;375–377:213–218. doi:10.1016/j.msea.2003.10.257

[3] Zhang RZ, Reece MJ. Review of high entropy ceramics: design, synthesis, structure and properties. J Mater Chem A. 2019;7:22148–22162. doi:10.1039/C9TA05698J

[4] Rost CM, Sachet E, Borman T, et al. Entropy-stabilized oxides. Nat Commun. 2015;6:8485. doi:10.1038/ncomms9485

[5] Bérardan D, Franger S, Meena AK, et al. Room temperature lithium superionic conductivity in high entropy oxides. J Mater Chem A. 2016;4:9536–9541. doi:10.1039/C6TA03249D

[6] Gild J, Zhang Y, Harrington T, et al. High-entropy metal diborides: a new class of high-entropy materials and a new type of ultrahigh temperature ceramics. Sci Rep. 2016;6:37946. doi:10.1038/srep37946

[7] Feng L, Fahrenholtz WG, Hilmas GE. Two-step synthesis process for high-entropy diboride powders. J Am Ceram Soc. 2019;00:1–7.

[8] Gild J, Wright A, Quiambao-Tomko K, et al. Thermal conductivity and hardness of three single-phase high-entropy metal diborides fabricated by borocarbothermal reduction and spark plasma sintering. Ceram Int. 2020;46:6906–6913. doi:10.1016/j.ceramint.2019.11.186

[9] Xu L, Guo WM, Zou J, et al. Low-temperature densification of high entropy diboride based composites with fine grains and excellent mechanical properties. Compos Part B-Eng. 2022;247:110331. doi:10.1016/j.compositesb.2022.110331

[10] Ye BL, Wen TQ, Nguyen MC, et al. First-principles study,fabrication and characterization of $(Zr_{0.25}Nb_{0.25}Ti_{0.25}V_{0.25})C$ high-entropy ceramics. Acta Mater. 2019;170:15–23. doi:10.1016/j.actamat.2019.03.021

[11] Feng L, Fahrenholtz W, Hilmas G. Low-temperature sintering of single-phase, high-entropy carbide ceramics. J Am Ceram Soc. 2019;102(12):7217–7244. doi:10.1111/jace.16672

[12] Jin T, Sang XH, Unocic RR, et al. Mechanochemical-assisted synthesis of high-entropy metal nitride via a soft urea strategy. Adv Mater. 2018;30:17075.

[13] Liu D, Wen TQ, Ye BL, et al. Synthesis of superfine high-entropy metal diboride powders. Scr Mater. 2019;167:110–114. doi:10.1016/j.scriptamat.2019.03.038

[14] Fu MS, Ma X, Zhao KN, et al. High-entropy materials for energy-related applications. iScience. 2021;24:102177. doi:10.1016/j.isci.2021.102177

[15] Liu D, Liu HH, Ning SS, et al. Synthesis of high-purity high-entropy metal diboride powders by boro/carbothermal reduction. J Am Ceram Soc. 2019;102(12):7071–7076. doi:10.1111/jace.16746

[16] Yu RW, Liu YW, Sun XH, et al. Composition engineering of high-entropy diboride nanoparticles for efficient catalytic degradation of antibiotics. Sci China Mater. 2023;66(9):3582–3591. doi:10.1007/s40843-023-2496-5

[17] Wen ZH, Meng H, Jiang SD, et al. Non-equimolar $(Hf,Zr,Ta,W)B_2$ high-entropy diborides enable superior oxidation resistance. Sci China Mater. 2023;66(8):3213–3222. doi:10.1007/s40843-023-2461-y

[18] Ma MD, Ye BL, Han YJ, et al. High-pressure sintering of ultrafine-grained high-entropy diboride ceramics. J Am Ceram Soc. 2020;103(12):6655–6658. doi:10.1111/jace.17387

[19] Tallarita G, Licheri R, Garroni S, et al. Novel processing route for the fabrication of bulk high-entropy metal diborides. Scr Mater. 2019;158:10–104. doi:10.1016/j.scriptamat.2018.08.039

[20] Zhang Y, Jiang ZB, Sun SK, et al. Microstructure and mechanical properties of high-entropy borides derived from boro/carbothermal reduction. J Eur Ceram Soc. 2019;39:3920–3924. doi:10.1016/j.jeurceramsoc.2019.05.017

[21] Failla S, Galizia P, Fu S, et al. Formation of high entropy metal diborides using arc-melting and combinatorial approach to study quinary and quaternary solid solutions. J Eur Ceram Soc. 2020;40:588–593. doi:10.1016/j.jeurceramsoc.2019.10.051

[22] Cao YB, Zhang X, Fan JM, et al. Synthesis of hierarchical Co micro/nanocomposites with hexagonal plate and polyhedron shapes and their catalytic activities in glycerol hydrogenolysis. Cryst Growth Des. 2011;11(2):47–479.

[23] Zhang DF, Sun LD, Zhang J, et al. Hierarchical construction of ZnO architectures promoted by heterogeneous nucleation. Cryst Growth Des. 2008;8(10):3609–3615. doi:10.1021/cg800143x

[24] Zhang KC, Zhang LH. Crystal growth. Beijing: China Science Press; 1981.

[25] Li PT, Wu YY, Liu X. Controlled synthesis of different morphologies of TiB_2 microcrystals by aluminum melt reaction method. Mater Res Bull. 2013;48:2044–2048. doi:10.1016/j.materresbull.2013.02.026

[26] Li C, Wu YY, Liu XF. Morphological evolution and growth mechanism of primary Mg2Si phase in Al-Mg2Si alloys. Acta Mater. 2011;59:1058–1067. doi:10.1016/j.actamat.2010.10.036

[27] Nie JF, Wu YY, Li PT, et al. Morphological evolution of TiC from octahedron to cube induced by elemental nickel. Cryst Eng Comm. 2012;14:2213. doi:10.1039/c1ce06205k

[28] Sun W, Dai FZ, Xiang HM, et al. General trends in surface stability and oxygen adsorption behavior of transition metal diborides (TMB_2). J Mater Sci Technol. 2019;35:584–590. doi:10.1016/j.jmst.2018.10.012

[29] Birkmann B, Hussy S, Sun G, et al. Considerations on facetting and on the atomic structure of the phase boundary in low-pressure solution growth of GaN. J Cryst Growth. 2006;297:133–137. doi:10.1016/j.jcrysgro.2006.09.011

[30] Shiohara Y, Endo A. Crystal growth of bulk high-Tc superconducting oxide materials. Mat Sci Eng R. 1997;19:1–86. doi:10.1016/S0927-796X(96)00198-2

[31] Liu D, Liu HH, Ning SS, et al. Chrysanthemum-like high-entropy diboride nanoflowers: A new class of high-entropy nanomaterials. J Adv Ceram. 2020;9 :339–348. doi:10.1007/s40145-020-0373-x

[32] Li PT, Li YG, Nie JF, et al. Influence of forming process on three-dimensional morphology of TiB_2 particles in Al-Ti-B alloys. T Nonferr Metal Soc. 2012;22:564–570. doi:10.1016/S1003-6326(11)61214-4

[33] Song SL, Zhang T, Xie C, et al. Growth behavior of TiB_2 hexagonal plates prepared via a moltensalt-mediated carbothermal reduction. J Am Ceram Soc. 2020;103:719–723. doi:10.1111/jace.16800

[34] Cui XL, Wu YY, Liu XF. Effect of Mn on growth mechanism and morphology evolution of CrB_2 in Al melt. Mater Lett. 2018;238:229–232.

[35] Mao HK, Li C, Dong Y, et al. The effect of Mn on particles morphology and property of 5 wt% TiB_2/Al-4.5Cu-0.4Mn alloys. J Alloy Compd. 2022;904:163907. doi:10.1016/j.jallcom.2022.163907

[36] Hu SJ, Li SB, Li HL, et al. Large-scale growth of TiB_2 hexagonal platelets. J Alloy Compd. 2017;690:930–935. doi:10.1016/j.jallcom.2016.08.208

[37] Li PT, Li C, Nie JF, et al. Gowth and design of LaB_6 microcrystals by aluminum melt reaction method. Cryst Eng Comm. 2013;15:411–420. doi:10.1039/C2CE26568K

[38] Gu JF, Zou J, Sun SK, et al. Dense and pure high-entropy metal diboride ceramics sintered from self-synthesized powdersviaboro/carbothermal reduction approach. Sci China Mater. 2019;62:1898–1909. doi:10.1007/s40843-019-9469-4

[39] Yang Y, Bi JQ, Sun KN, et al. Novel $(Hf_{0.2}Zr_{0.2}Ta_{0.2}V_{0.2}Nb_{0.2})B_2$ high entropy diborides with superb hardness sintered by SPS under a mild condition. Ceram Int.

2022;48:30859–30867. doi:10.1016/j.ceramint.2022.07.040

[40] Feng L, Fahrenholtz WG, Hilmas GE, et al. Effect of Nb content on the phase composition, densification, microstructure, and mechanical properties of high-entropy boride ceramics. J Eur Ceram Soc. 2021;41:92–100. doi:10.1016/j.jeurceramsoc.2020.08.058

[41] Qin MD, Gild J, Wang HR, et al. High-entropy rare earth tetraborides. J Eur Ceram Soc. 2020;40:4348–4353. doi:10.1016/j.jeurceramsoc.2020.03.063

[42] Feng L, Monteverde F, Fahrenholtz WG, et al. Superhard high-entropy AlB_2-type diboride ceramics. Scr Mater. 2021;199:113855. doi:10.1016/j.scriptamat.2021.113855